Thin–Walled Structures 218 (2026) 114104

Contents lists available at ScienceDirect

Thin-Walled Structures

journal homepage: www.elsevier.com/locate/tws

Full length article

PZT piezoceramic nanofibers for impact localization in composite laminates

Giacomo Selleri [a,*], Maria Elena Gino [b], Federica Zonzini [c], Luca De Marchi [c], Maria Letizia Focarete [b], Davide Fabiani [c], Andrea Zucchelli [a], Tommaso Maria Brugo [a]

[a] Department of Industrial Engineering, University of Bologna, Viale Risorgimento 2, 40136 Bologna, Italy
[b] Department of Chemistry "Giacomo Ciamician" and INSTM UdR of Bologna, University of Bologna, via Selmi 2, 40126 Bologna, Italy
[c] Department of Electrical, Electronic, and Information Engineering, University of Bologna, Viale Risorgimento 2, 40136 Bologna, Italy

ARTICLE INFO

Keywords:
Composites
PZT nanofibers
Piezoelectric
Impact localization

ABSTRACT

Structural Health Monitoring (SHM) of composite laminates often relies on embedded sensors, which can detrimentally compromise the material's mechanical integrity. In contrast, micro and nanomaterials have been shown to exert minimal impact on the mechanical performance of laminates while providing effective sensing capabilities for compressive, tensile, and tactile loads. Nevertheless, the detection of elastic wave propagation continues to depend on ceramic piezoelectric lead zirconate titanate (PZT) sensors. This study presents an innovative approach by integrating PZT nanofibers directly into the composite laminate structure, effectively combining the superior piezoelectric properties of PZT with the advantages of a nanostructured, minimally intrusive material. Specifically, PZT nanofibers are strategically interleaved and positioned at the corners of a rectangular glass fiber reinforced plastic (GFRP) panel (30 × 20 cm). Upon impact on the laminate surface, the high sensitivity of the PZT nanofibers enables the detection of elastic waves propagation, generating a piezoelectric signal that allows for precise impact localization through a triangulation algorithm. Compared with a traditional panel with commercial PZT disks interleaved, the nanostructured panel exhibits a higher impact localization error (2.50 ± 2.46 cm versus 3.74 ± 2.84 cm), while exerting less influence on its mechanical properties. Indeed, low-velocity impact tests confirm the superior impact resistance of the nano-modified laminate compared to its counterparts with traditional PZT sensors.

1. Introduction

The use of composite materials is rapidly growing in various engineering fields, such as automotive and aerospace, due to their stiffness and excellent mechanical strength. Combining fiber materials (i.e., carbon or glass fiber) with a polymeric epoxy resin gave rise to the family of Fiber Reinforced Plastics (FRPs), widely used for lightweight structures. The major drawback of the composite materials originates from their laminar morphology, which represents a potential issue in the case of impacts or out-of-plane loads [1]. When the impact occurs, cracks can be generated and propagate between the laminate plies as delamination without any visual recognition, thus leading to catastrophic failures of the material. For these reasons, different strategies have been explored to monitor any damage to the composite material and to prevent structural failures. Structural Health Monitoring (SHM) systems can monitor manifold quantities, such as stress, strain or vibrations, in real-time, ensuring improved structural safety and timely retrofitting actions. In the last period, substantial efforts have been made to design multifunctional composite materials which conjugate the mechanical properties of the laminates with sensing capabilities. Generally, two main strategies have been explored: manufacturing self-sensing composite materials based on different sensing principles (e.g., electrical resistance or capacitance sensing) or integrating various types of sensors into the laminate.

Various techniques have been investigated to fabricate a self-sensing structure by exploiting non-invasive SHM methods [2]. Among these, the electrical resistance sensing method is based on measuring the change of electrical conductivity of the Carbon Fiber Reinforced Plastic (CFRP) due to mechanical deformation, strain or temperature variation. Since the conductivity is not isotropic and depends on the orientation of the carbon fibers, its variation can, therefore, be correlated to damages and fiber fractures [3–5]. Similarly, the capacitive-based sensing technique relies on the effect of damage, stress or strain on the capacitance of the composite. Consequently, the sensing capability of the composite

* Corresponding author.
E-mail address: giacomo.selleri2@unibo.it (G. Selleri).

https://doi.org/10.1016/j.tws.2025.114104
Received 20 June 2025; Received in revised form 29 September 2025; Accepted 12 October 2025
Available online 13 October 2025

strongly depends on the permittivity of the dielectrics between the CFRP plies [6]. Efforts have been made to improve the sensitivity of the laminates – both for the resistive and capacitive mechanisms - by adding nanofillers in the polymeric matrix, such as carbon nanotubes (CNs) [7] or titania fillers [8]. However, the significant drawbacks of those techniques are related to their electrical contacts, which can strongly affect the electrical measurements and the power supply needed.

Other sensing strategies rely on the use of sensors [9], such as piezoelectric [10], Fiber Bragg Grating (FBGs) [11] and resistive sensors [12,13].

The use of FBGs sensors has been widely investigated in literature for damage localization purposes in composite laminates. For an easier manufacturing procedure and the ability for visual inspection of the sensor, they can be attached on the surface of the laminate, usually with epoxy adhesive. For instance, an array of four multiplexed fiber Bragg grating (FBG) sensors attached on a composite plane was used to validate the impact localization algorithm [14]. Other works demonstrated the effectiveness of FBGs attached on CFRP laminates to detect delamination and real-time impacts [15–17]. Alternatively, for a precise monitoring of the interlaminar strain and to prevent damaging from environmental conditions, FBG sensors can be embedded between the fiber layers [11]. Impact localization, strain-temperature sensing and cure-induced strain gradient monitoring were successfully performed by embedding FBGs within CFRP laminate plies [18–20]. However, dynamic load tests could induce debonding between the optical fiber and the composite [21], and eye-shaped resin pocket can form, inducing a stress concentration at the interface [22].

Piezoelectric sensors have been widely exploited for impact localization and SHM. According to the sensors disposition, the received impact signals can be processed with various techniques to determine the impact point. For instance, Deng et al. presented a multi-frequency probabilistic imaging fusion method for localizing impacts on aircraft composite structures, by using a network of distributed sensors [23]. Additionally, piezoelectric sensors were mounted on the structure to implement an impact localization method based on Bayesian estimation and weighted averaging [24]. Demi et al. proposed a new damage localization approach on a reinforced concrete (RC) slab using electromechanical impedance/admittance (EMI/EMA) technique, by mounting an array of surface-bonded PZT patches [25,26]. Nevertheless, as for FBGs sensors, the attachment of the sensor on the surface of the composite material is still not an entirely accepted solution as it may suffer from degradation and detachment. For these reasons, the embedding of the sensors in the stacking sequence during composite manufacturing is becoming a strategic research topic. However, the integrated sensing element represents a defect that can reduce the laminate's mechanical properties. The integration mechanism of piezoelectric sensors in composite materials, such as ceramic PZT or polymeric polyvinylidene fluoride (PVdF), has been deeply studied regarding both sensing capabilities and mechanical properties of the laminate [27,28]. By placing PZT disks in strategic positions of the structure (i.e., attached on the CFRP surface [29] or in the midplane of the composite material [30]), the impact localization performances have deeply been studied in different works. The high sensitivity of embedded sensors for acoustic emission (AE) monitoring in composite structures was demonstrated, for example, in [31–33].

Moreover, the impact of different PZT sensor dimensions on the elastic waves detection sensitivity was investigated for PZT disks integrated between the laminate plies [34]. However, due to the fragile and brittle nature of the ceramic PZT, sensor fractures could occur, and delamination could originate and propagate between the laminate plies. The use of piezo-polymers, such as poly(vinylidene fluoride–trifluoroethylene) (PVdF-TrFE), could be a promising solution due to its flexibility, but still a degradation of the structural integrity of the host composite laminate was observed [29] due to the interface strength between the hosting matrix and the fluorinated polymer. For these reasons, in the last period, many scientific works have focused on the possibility of integrating nanostructured piezoelectric materials in composite laminate. For instance, via the electrospinning technique, it is possible to fabricate a piezoelectric nanofibrous membrane of PVdF-TrFE, which can be embedded between the plies of the composite material [35,36]. Thanks to the high porosity of the nanofiber membrane, the epoxy resin penetrates the air gaps of the layer so that each nanofiber is surrounded by the polymeric matrix [37]. Unlike a bulk polymeric film, the integration mechanism of a nanofibrous membrane does not negatively impact the mechanical properties of the laminate; instead, it demonstrates an increase in the mode-I fracture toughness [38]. Similarly, studies have been done to substitute PZT commercial disks with alternative shapes, such as PZT powder ([39,40]) or PZT microfibers [41], to be interleaved between the GFRP plies. These techniques are promising strategies to fabricate self-sensing composite materials which combine a high sensitivity – thanks to the high piezoelectric strain coefficient d_{33} of the ceramic PZT - with a limited impact on the inherent strength of the laminate.

In this context, this works proposes an innovative design of self-sensing composite panel for impact localization with PZT nanofibers embedded (PZT_nf). The main purpose is to conjugate the high piezoelectric properties of PZT with the mechanical benefits of nanostructured sensing elements. This novel approach, in fact, proposes an autonomous, self-powered laminate designed to detect the propagation of elastic waves while exerting minimal impact on the panel's mechanical properties. Specifically, four PZT nanofibrous membranes were strategically placed at the corners of a 20 × 30 cm rectangular panel to define the perimeter of the sensing area. Upon impact within this area, elastic waves travel to the nanofibers, generating piezoelectric signals that allow for precise impact localization through a triangulation algorithm. For comparison, a GFRP composite panel embedded with commercial interleaved PZT sensors (PZT_disk) was also fabricated. A detailed assessment of the two panels was carried out, focusing on both impact localization and mechanical properties, to highlight the advantages and limitations of the proposed technology.

2. Materials and methods

The manufacturing process of the composite panels for the autonomous self-powered impact localization started with the fabrication of the PZT nanofibers (Section 2.1), which were subsequently embedded and poled in the GFRP panels (Section 2.2). The impact localization and mechanical performances of the panels were then evaluated, as described in detail in Section 2.3. Fig. 1 summarizes the proposed framework and main steps adopted in this work.

2.1. PZT nanofibers fabrication

PZT ceramic nanofibers were fabricated through sol-gel electrospinning, according to the three main steps described in this section. The process starts with the PZT precursor solution preparation (Section 2.1.1), which is mixed with the polymer carrier Poly(vinyl acetate) (PVAc, MW = 500.000 Da) to be suitable for the electrospinning process (Section 2.1.2). In particular, gelification must be avoided, and the sol-gel solution's entanglement must be increased to overcome the electrostatic forces developed between the needle and the collector during the electrospinning process. The last issue has been solved by adding a carrier polymer to the PZT precursor solution to increase the concentration and enhance the viscoelastic performance due to the chain entanglements. Finally, a thermal treatment (Section 2.1.3) was carried out on the obtained as-spun nanofibers to allow the growth of dimensionally stable PZT nanofibers.

2.1.1. Synthesis of PZT precursors solution

The entire synthesis procedure is reported in this section and was followed to produce a 50 mL of stable PTZ precursor solution [42,43].

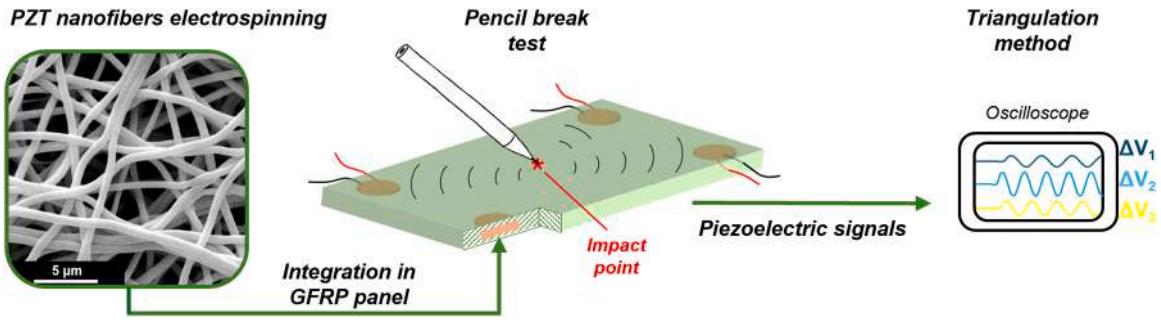

Fig. 1. Proposed framework: from PZT nanofibers to the fabrication of the self-sensing composite panel and impact localization testing.

Zirconium (IV) n-propoxide 70 wt.% solution in 1-propanol (0.0156 mol) and Titanium (IV) isopropoxide 97 % (0.0144 mol), were mixed and dissolved in acetic acid (7 mL). Meanwhile, lead (II) acetate trihydrate (0.0372 mol) was dissolved in acetic acid (14 mL), the solution was stirred at a temperature of 100 °C for 30 minutes, and then it was left to cool to room temperature (RT). Before forming a homogeneous lead and metal alkoxide solution, 2-methoxyethanol anhydrous 99.8 % (15 mL) was added. The whole system was heated at 80 °C and left stirring for 1 hour. Afterwards, another portion of 2-methoxyethanol (14 mL) was added and the solution was left stirring under reflux overnight at 80 °C. Finally, the solution was cooled down to RT and then vacuum-filtered with a Büchner funnel. All reagents and solvents were purchased from Sigma Aldrich[1], apart from glacial acetic acid, which was purchased from Carlo Erba[2]. All reagents and solvents were used without further purification.

2.1.2. Electrospinning process

The process to obtain pristine PZT nanofiber starts with the precursor solution, which must be stable enough and possess the proper viscosity to be subjected to electrospinning. The precursor solution was mixed with PVAc as a carrier polymer at a 10 % w/v concentration to reach these goals [44–46], as schematically shown in Fig. 2a. A solution was prepared with 500 mg of PVAc, dissolved in 5 mL of PZT precursor solution. The solution was stirred at RT for 24 hours and then electrospun (Fig. 2b). The electrospinning apparatus (Spinbow S.r.l., Bologna, Italy[3]) comprises a high voltage generator (SL 50 P 10/CE/230 Spellman, New York, USA[4]), a syringe pump (KDScientific Inc., Massachusetts, USA[5]), a plastic syringe containing the polymeric solution and a stainless-steel blunt-ended needle (inner diameter= 0.5 mm). The needle was connected to the high voltage generator (16 kV), and a cylindrical low-speed rotating drum was used as the ground collector (diameter=5 cm, length=10 cm, angular speed = 70 rpm). The distance between the needle and the collector was set at 16 cm, and the process took place at RT and relative humidity of 50 %, with a solution flow rate of 16 μL/h.

2.1.3. Thermal treatment

The as-spun PVAc/PZT nanofibers were subjected to a sequence of heat treatments to obtain ceramic PZT nanofibers, as summarized in Fig. 2c. First, i) the nanofiber mat was heated for 12 h at 115 °C in air; then ii) the temperature was increased up to 210 °C for 12 h; finally, iii) the nanofibers were stored for 1 h at 700 °C in air and quenched. The temperature ramps to move to the next heating step were set at 10 °C/min [44–46].

The heat-treatment processes were optimized to prepare PZT nanofibers in the perovskite phase by heating steps, which allowed a slow shrinkage of the electrospun mat, a slow thermo-oxidative degradation of carrier polymer and a growth of PZT crystal grains.

2.2. Self-sensing laminate fabrication

Two types of sensing plates were manufactured by interleaving two different types of piezoelectric elements: PZT commercial disks (Murata, 7BB-20-6L0 made of Piezotite® P-7B piezoelectric material[6]) and PZT nanofibers produced by sol-gel electrospinning process. The piezoelectric sensors were disposed in the four angles of the GFRP plate, according to the stacking sequence described in Section 2.2.1 and then polarized (Section 2.2.2). Such a disposition of the sensors was exploited for impact localization by elastic wave detection.

2.2.1. Lamination and curing

Both laminates were composed of 10 woven GFRP prepreg plies (E-glass 8H Satin 300 g/m^2 - epoxy matrix, VV300S - DT121H-34 DeltaPreg S.p.A., 300 × 200 × 0.26[7]) mm^3. In particular, the stacking sequence of the laminate with the commercial PZT disk (named PZT_disk, Fig. 3a) is [(GFRP-0°)$_2$/ PZTcom/ (GFRP-0°)$_8$] with a total thickness of 3.1 mm in correspondence of the sensors. On the other hand, the stacking sequence of the laminate with PZT nanofibers (named PZT_nf, Fig. 3b) is [(GFRP-0°)$_1$/ Brass /(GFRP-0°)$_1$ /PZTnf/ (GFRP-0°)$_1$ / Brass / (GFRP-0°)$_7$] with a total thickness of around 3.2 mm in correspondence of the sensors. Instead, the thickness of the portion of the laminates without the sensing

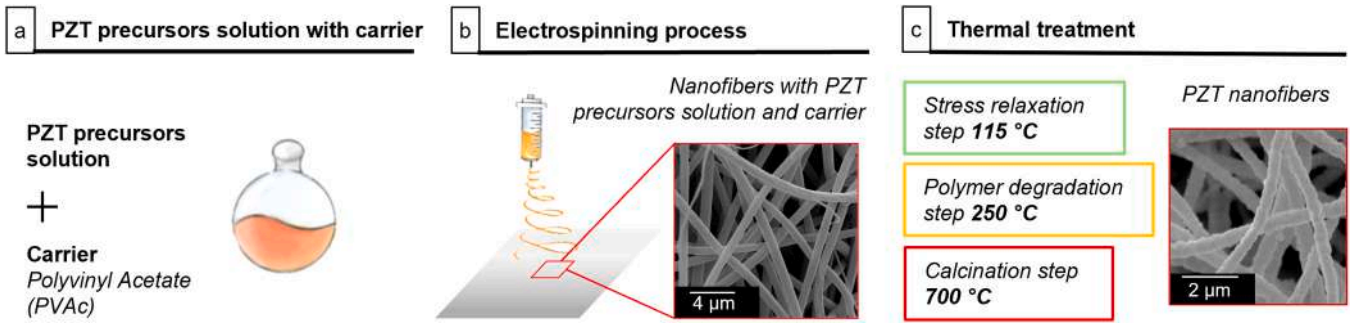

Fig. 2. Fabrication steps of the PZT nanofibers: a) solution with PZT precursors and carrier; b) electrospinning process and c) thermal treatments.

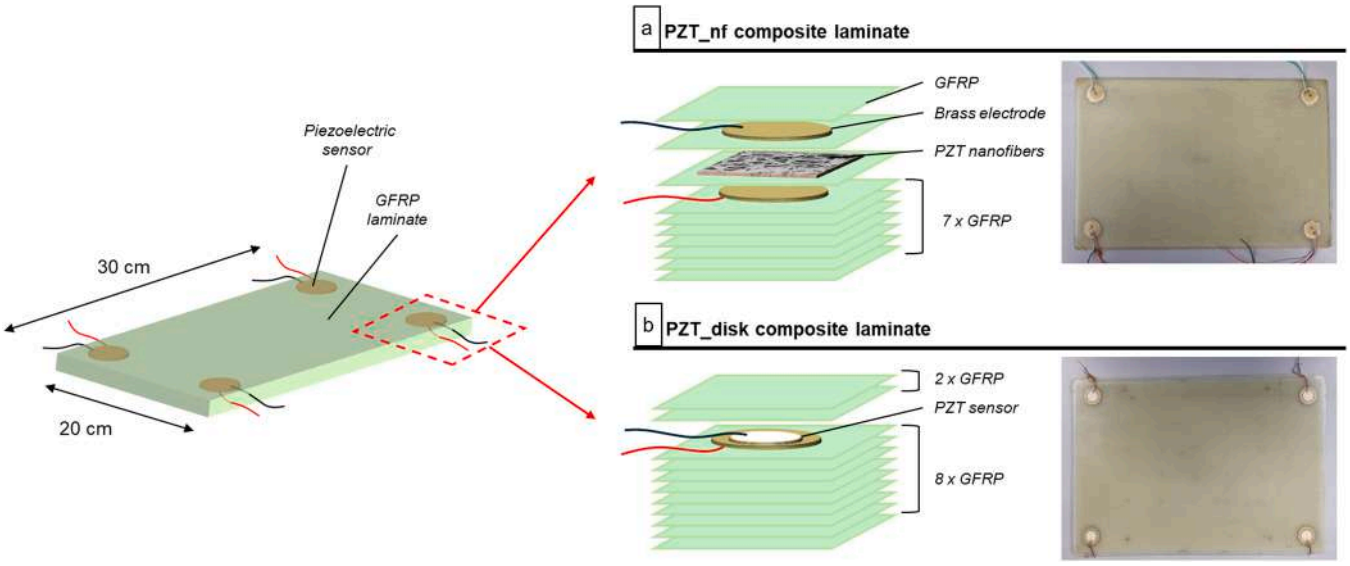

Fig. 3. Pictures and schematic representation of the stacking sequence of the (a) PZT nf and (b) PZT disk self-sensing composite panels.

elements is equal to 2.7 mm. Considering the PZT_nf panel, the circular brass sheets (⌀ 14 × 0.1 mm^2 for the upper electrode and ⌀ 20 × 0.1 mm^2 for the bottom one) have the electrical function of collecting the piezoelectric signal generated by PZT nanofibers (600 g/m^2). Before stacking, the brass sheets were treated with sandpaper (P220), and signal cables with Teflon jackets were soldered. The lamination staking sequences were chosen to have piezoelectric elements at the same plane of the laminate, i.e., between 2nd and 3th plies of GFRP.

After stacking, the plates were cured in an autoclave using a vacuum bag technique, following the custom 3-step curing cycle described in [35]. The epoxy resin's glass transition temperature (T_g) after curing equals 132 °C.

2.2.2. Poling

To induce piezoelectricity in ferroelectric ceramics, an external electric field must be applied to align the ferroelectric domains in the direction of the field. Since the PZT commercial disks embedded in the PZT disk composite plate are characterized by piezoelectric behavior, as they were supplied already polarized, the polarization process was performed only on the PZT_nf composite laminate. The high voltage (HV) generators (FUG HCN 35-35000 Hochspannungs-Netzgerat[8]) were used to apply an electric field of 4 kV/mm (higher electric fields resulted in electrical breakdown) to each PZT nanofibrous layer for 24 hours at 120 °C to facilitate the dipoles to move accordingly to the electric field direction. Subsequently, the temperature decreased to RT, and the high-voltage generator was switched off. To entirely remove the residual electrostatic charges generated during the polarization process and trapped within the composite material, both electrodes were connected to the ground at 40 °C overnight.

It is worth highlighting that the electric field was applied directly to the composite material and not only the PZT nanofibers. Therefore, the electric field is distributed unevenly between the two phases (PZT and GFRP) according to their electrical properties and volumetric fractions in the region between the high voltage and ground electrodes. Likely, such a poling method does not lead to a complete polarization of the PZT nanofibers, as the dielectric strength of the matrix represents a physical limit, but it is still effective to obtain measurable piezoelectric output signals. This mechanism has been described in detail in previous works [47,39].

2.3. Characterization and testing

The morphology and microstructure of the nanofibers were analyzed by Scanning Electron Microscopy (SEM, Phenom ProX), using a Philips 515 microscope at an accelerating voltage of 20 kV. Samples were fixed on an aluminium stub with a conducting bi-adhesive tape and sputter coated with gold before analysis. Images were analyzed with Image J software, and the distribution of nanofiber diameters was determined by measuring about 300 fibers. The results were provided as the average diameter ± standard deviation.

The X-ray diffractograms of the PZT were collected using an X'PERT diffractometer pro with PIXcell 1D as a detector: the 2θ range was from 15° to 60°, with a step size of 0.03° and a time of 60 s per step. The radiation used was the CuKα (40 mA, 40 kV) with a wavelength of 1.54 Å. The relevant peaks were analyzed using the program X Pert High Score. Thermogravimetric analyses (TGA) were carried out using a TGA Q500 thermogravimetric analyzer (TA Instruments). Analyses were performed on 10-15 mg samples, from RT to 800 °C, at a heating rate of 10 °C/min, under air flow.

The electrical properties of the sensing composite laminates were evaluated in Section 2.3.1 regarding piezoelectric sensitivity and capacitance measurements. Afterwards, the laminates were impacted on different known points of their surface, and the triangulation method based on elastic wave propagation was adopted to identify the position of the impact, as described in Section 2.3.2. Finally, low-velocity impact tests were performed on the laminates to compare the effect of interleaving piezoelectric nanofibers with respect to PZT commercial sensors on the mechanical resistance of the composite materials (Section 2.3.3). All tests were performed in laboratory conditions in controlled temperature (28 °C) and humidity (40 %) levels lasting over the entire session.

2.3.1. Piezoelectric and dielectric characterization

The piezoelectric strain coefficient d_{33} of each composite piezoelectric portion of the laminate can be measured according to the method described Appendix B, by reversing Equation (1):

$$V(t) = \frac{Fd_{33}}{C} sin(\omega t) \quad (1)$$

where V is the output voltage, F is the force applied and C is the capacitance of the piezoelectric sensor.

Therefore, the sensors of both the PZT_disk and PZT_nf composite

laminates were electromechanically characterized by applying a compressing sinusoidal load oscillating between 0 and 90 N at 20 Hz. The linear motor (LinMot®) was equipped with Teflon indenter of 1 cm diameter and a 300 N load cell (Model 1042, Single point load cells, Tedea-Huntleigh) for measuring force. The indenter was used to apply a force in the central point of each embedded sensor, as shown in Fig. 4. The cables of the piezoelectric signal (white and green cables) were connected to an INA118 (high input impedance R_{in} =10 GΩ) [36,39]. The load cell and piezoelectric signals were simultaneously acquired at a frequency of 0.5 kHz by a digital oscilloscope (Tektronix DPO 5034). A copper tape was placed on both the surfaces of the sensing portions of the laminates and it was connected to the ground, hence erasing any external noise or triboelectric signals that could affect the piezoelectric output measurement. The sensitivity (mV/N) was then calculated for each sensor as the ratio between the peak-to-peak output voltage and the peak-to-peak value of the compressive force.

The impedances of the sensing laminates were measured in the 10^{-1}-10^{3} kHz range using a precision impedance analyzer (Agilent 4294A). The measurements were performed on each of the four sensors integrated in the GFRP plates. The capacitances were determined by interpolating the impedance vs. frequency curve using the linear equation of the RC circuit.

2.3.2. Impact localization method

Both the PZT disk and the PZT nf plates were excited with low energy impacts by breaking a 0.5 mm diameter pencil lead on different positions of their surface. The reason for adopting this testing strategy is that it can emulate, in a controlled and reproducible manner, the effects of stress and microscopic deformation caused by cracks or defects. The pencil lead break (PLB) test, also known as Hsu-Nielsen test, consists of breaking a 0.5 mm (alternatively 0.3 mm) diameter pencil lead approximately 3 mm (± 0.5 mm) from its tip by pressing it against the surface of the piece[10]. While the methodology is well established and regulated by precise testing procedures [48], variations in lead type, size, and break angle can imply differences in the generated AE event in terms of released energy, which is not possible to reproduce systematically. In our case, to minimize the potential problems due to these experimental issues, we made use of custom AE instrumentation, including a purposely designed PLB pencil which forces a 30° inclination angle during every experiment, being the lead type and diameter equal.

Therefore, it is conventionally exploited to analyze the sensitivity of piezoelectric sensors in response to these subtle phenomena [49]. A total amount of 20 impacted positions was selected, with a grid pattern of 4 × 5 (vertical and horizontal spacing of 30 mm and 40 mm, respectively). As shown in Fig. 5a, the areas of the sensors in the 4 angles of the laminates were covered with copper tape connected to the ground to remove frictional and triboelectric noises.

It is worth recalling that three sensing positions are sufficient to effectively localize a target in a bi-dimensional mesh of passive sensors via triangulation algorithms [50]. Therefore, piezoelectric signals were

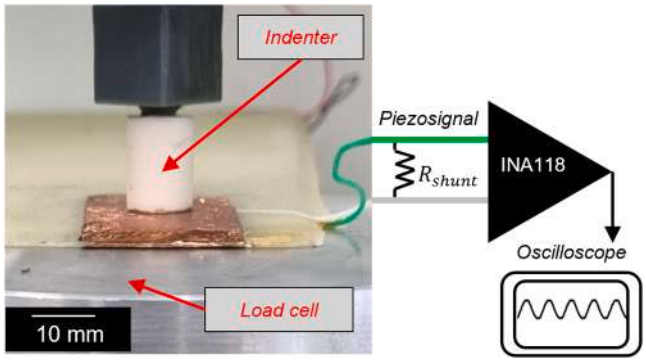

Fig. 4. Piezoelectric signal output measurement setup.

detected by three (S1, S3 and S4) out of the four sensors interleaved in the laminate. Data were acquired by means of a Tektronix oscilloscope set at a sampling frequency of 25 MHz and used during an offline post-processing phase for localization performance evaluation, according with the procedure outlined in Fig. 5b.

Let's assume that $\widehat{d}$ and $\widehat{\theta}$ represent the Euclidean distance and angle of impact with respect to a reference sensing position, coincident with S4. Thus, the impact position ($\widehat{x}_P$, $\widehat{y}_P$) can be estimated as:

$$\begin{cases} \widehat{x}_P = x_{S_4} + \widehat{d}\cos\widehat{\theta} \\ \widehat{y}_P = y_{S_4} + \widehat{d}sen\widehat{\theta} \end{cases} \quad (2)$$

with $\widehat{d}$ and $\widehat{\theta}$ being dependent on the Time-of-Arrival (ToA, time at which the signal arrives at the receiving sensor S4) and c_g (wave speed related to the fastest propagation mode). To this end, the Akaike Information Criterion has been employed, given its superior performance in ToA retrieval while processing signals from plate-like structures [51]. The wave propagation speed c_g was measured by Pitch-catch method in different directions with the setup reported in Fig. 5c. A further PZT commercial disk was attached by means of a couplant gel on different positions on the laminate surface and it was used as actuator to generate an impulse. A synchronized signal was acquired by one of the four PZT integrated sensors. The antisymmetric mode (orthogonal) was detected due to the higher amplitude compared to the symmetric one (in-plane). The average antisymmetric wave propagation of the graph of Fig. 5c is 1026 m/s with a maximum variation of 5 % over the 90° measured range. Therefore, the propagation speed c_g behavior can be approximated as in-plane isotropic. Starting from these quantities, the pair ($\widehat{x}_P$, $\widehat{y}_P$) was eventually obtained via the triangulation algorithm in [50].

2.3.3. Low-velocity impact

Low-velocity impact tests were carried out on the sensitive part of the piezoelectric self-sensing composite laminates using a drop-weight machine. Four 50 × 50 mm^2 specimens were extracted from both the PZT disk and PZT nf laminates by cutting a portion of the original self-sensing composite plates. The geometry of the obtained specimens was such that the sensors (PZT nanofibers layers and PZT commercial disks) were located in the center. Moreover, four GFRP pristine specimens were stacked with a stacking sequence of $[GFRP\text{-}0^\circ]_{12}$ and cured with the same curing process described in Section 2.2.1, without any piezoelectric element interleaved. The purpose was to investigate the effect of the PZT nanofibers interleaving on the mechanical resistance of the laminate with respect to a GFRP pristine laminate and a composite material with PZT commercial disks interleaved. The pristine composite material was fabricated by stacking 12 layers of GFRP to compensate for the thickness of the PZT nf laminate in the impacted point. Indeed, since the portion of the composite plates with PZT nanofibers interleaved was thicker than the rest of the laminate, a consistent evaluation of the mechanical resistance requested laminates with the same thicknesses.

The tests were performed with the setup described in [39] following the ASTMD7136 standard modified with a circular hole 20 mm diameter, as shown in Fig. 6. Three different levels of impact kinetic energy equal to 3, 6 and 9 J were chosen to evaluate the effect of the interleaving of the piezoelectric sensors on the impact resistance of the hosting laminate. After impact, cross-section micrograph analyses of the damaged zone were performed. Furthermore, one specimen of each composite laminate typology was not impacted to evaluate the morphology of the embedded piezoelectric sensors.

3. Results and discussion

The characterization of the manufactured composite panels is described in the following. First, the morphology and crystalline phases of the PZT nanofibers are discussed Section 3.1, and their integration within the GFRP plies is evaluated in Section 3.2. Afterwards, the PZT nf

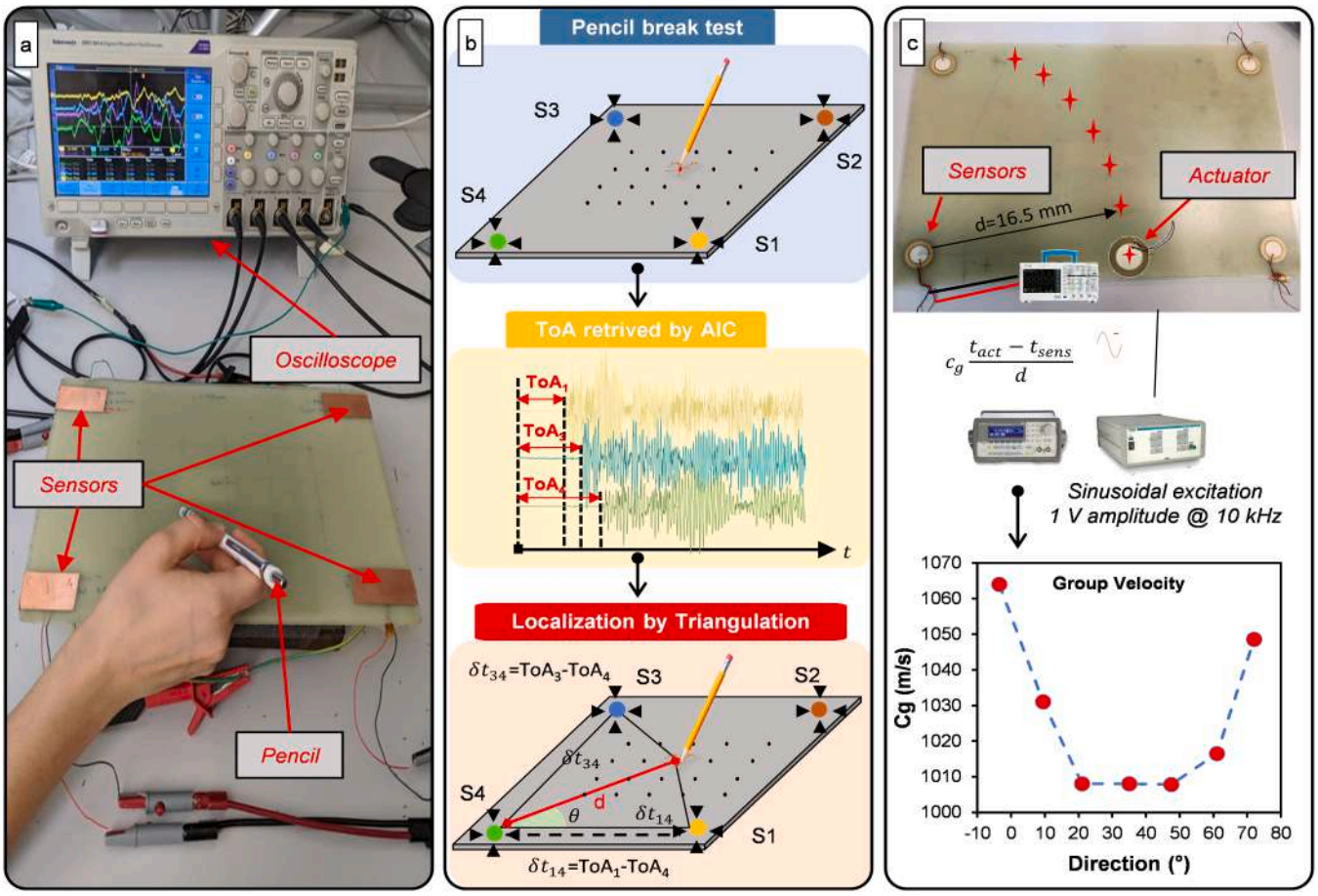

Fig. 5. (a) Example of pencil lead break test on the PZT disk plate; b) schematic representation of the impact localization testing procedure: from pencil lead break tests to impact localization via triangulation, passing through an intermediate step of ToA identification; c) c_g measurement method.

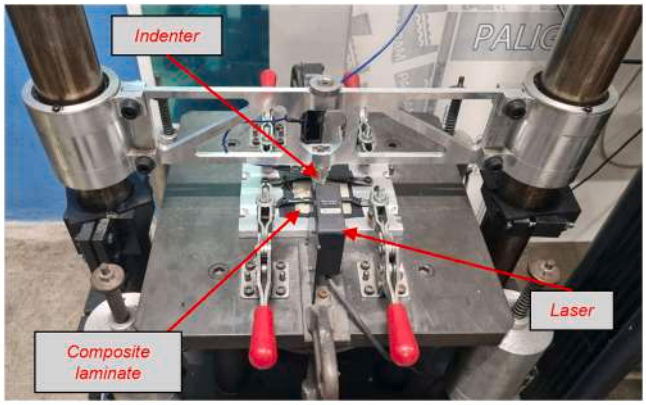

Fig. 6. Low-velocity impact setup.

and the PZT disk composite panels are compared in terms of piezoelectric (Section 3.3), impact localization (Section 3.4) and impact resistance (Section 3.5) performances.

3.1. PZT nanofibers characterization

The morphology of the obtained PZT nanofibers was analyzed using SEM. Fig. 7a shows the as-spun PZT nanofibers, whereas the nanofibers after the thermal treatments of section are shown in Fig. 7b. Smooth and bead-free as-spun fibers with an average diameter of 620 ± 80 nm were obtained. This satisfactory result can be attributed to the good spinnability of the PZT/PVAc solution used during the electrospinning process. The SEM image after the thermal treatment shows nanofibers tightly bonded to each other along the axial direction, creating a nanofibrous mat with a dense structure, with an average fiber diameter of 340 ± 120 nm. If compared to the as-spun nanofibers, this considerable diameter shrinking can be attributed to the removal of the carrier polymer by thermo-oxidative degradation and to the densification of the PZT crystal structure. The overlay of the diffractograms (Fig. 7c) highlights the absence of crystalline phases in the as-spun nanofibers (red line), while the pure perovskite phase of PZT nanofiber (black line) is completely formed after thermal treatments, as confirmed by the values of 2Θ for the peaks located at 21.5°, 30.7°, 37.9°, 44.2°, 49.6°, 54.9°, in agreement with literature data [52–54]. In Fig. 7d, the TGA shows that PZT dried at 110 °C has strong multistep decomposition up to ~600 °C, while drying at 210 °C reduces residues but still leaves organics. After calcination at 700 °C the powder is thermally stable, confirming oxide formation. Main losses occur <150 °C (moisture), 150–400 °C (organics), and 400–600 °C (carbonates/precursors). Above 700 °C the oxide is stable, though PbO volatilization may begin. Thus, controlled burnout and calcination at ~700 °C are essential to obtain stable PZT while minimizing porosity and preserving stoichiometry.

3.2. Micrograph analyses

The integration of the ceramic piezoelectric nanofibers with the GFRP plies was investigated by optical (Fig. 8a) and SEM (Fig. 8b and Fig. 8c) micrograph analyses of the cross-section of a PZT nf sensor before impact. The stacking sequence of the PZT nf sensor is clearly observable in the optical micrograph image of Fig. 8a, where the PZT

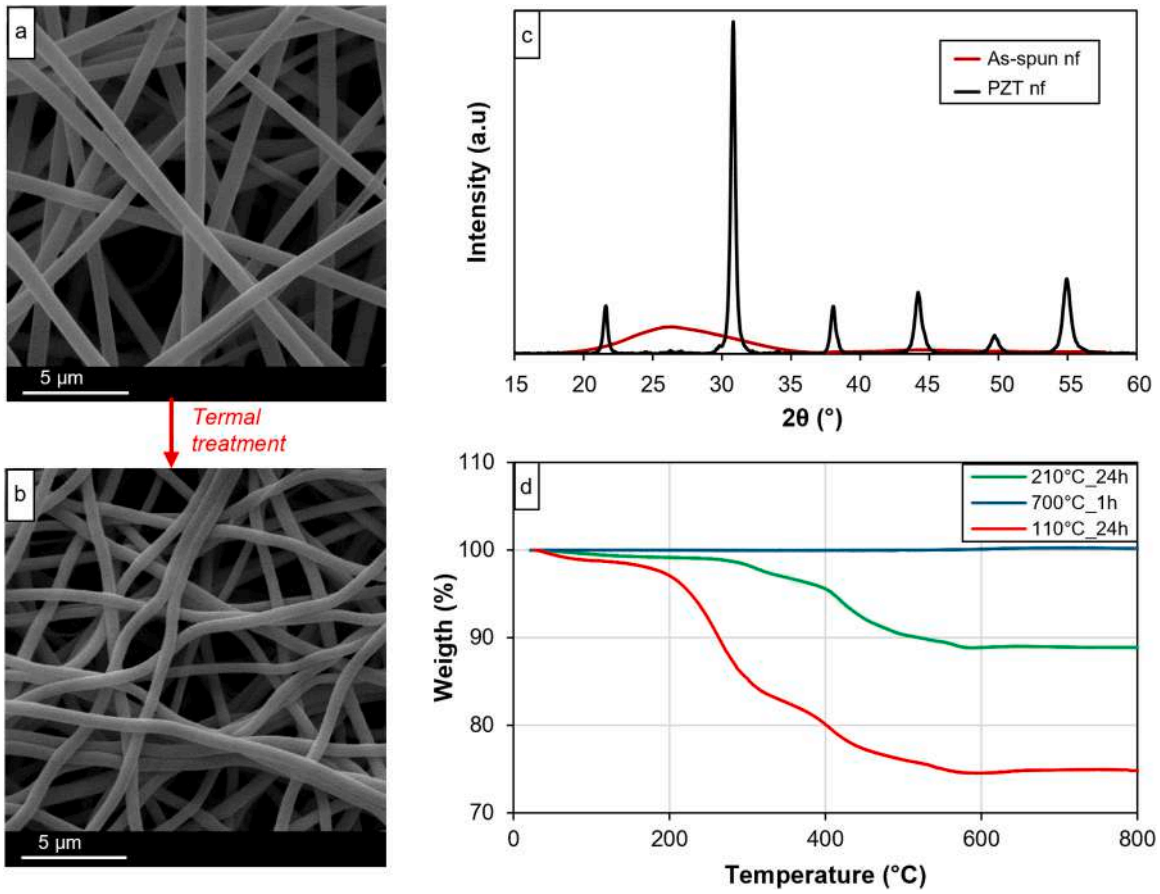

Fig. 7. Morphological and structural characterization of the PZT nanofibers. SEM images of a) as-spun nanofibers and b) thermally treated nanofibers; c) XRD diffractograms of as-spun nanofibers (red line) and nanofibers after thermal treatment (black line); d) TGA curves for different heat treatments.

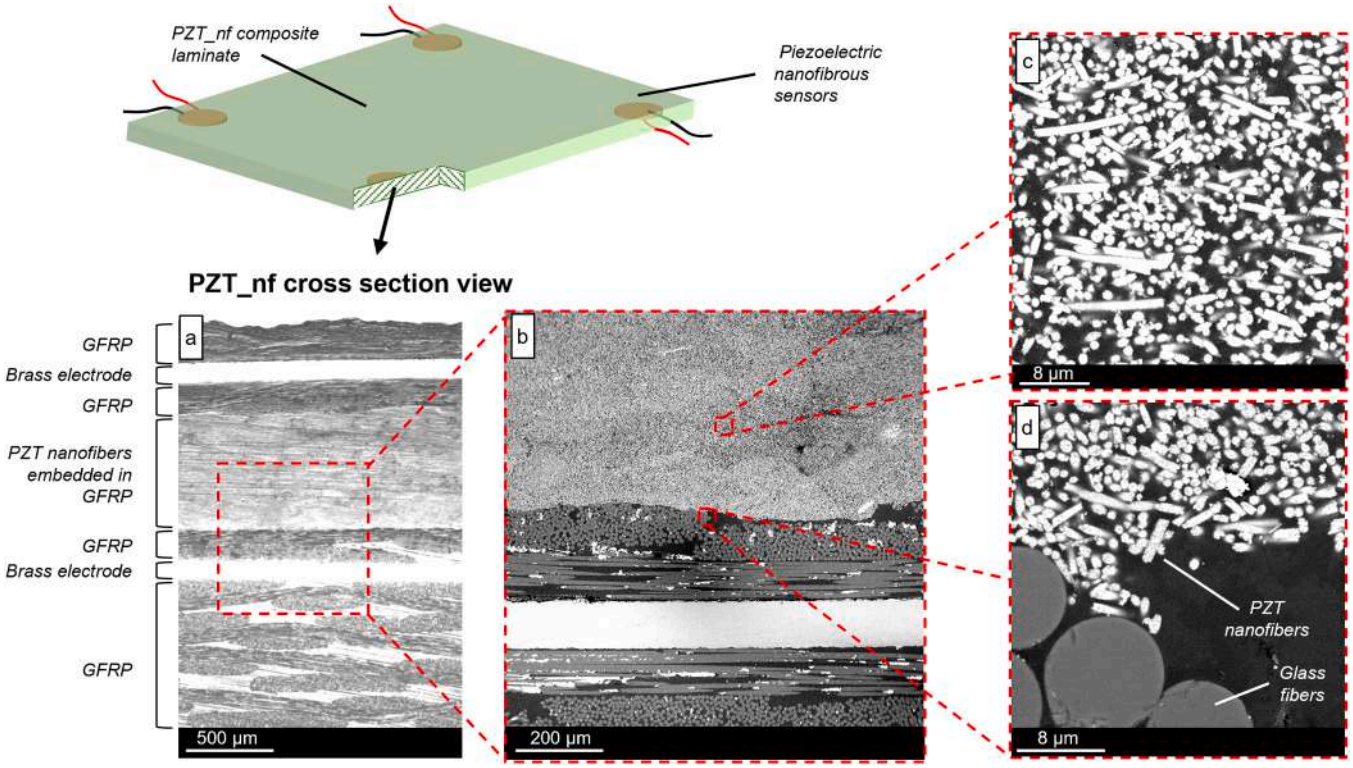

Fig. 8. a) Optical micrograph of the PZT_nf composite laminate; b-d) SEM magnification of the piezoelectric nanofibers embedded in the epoxy matrix.

nanofibers are sandwiched between two adjacent GFRP plies and embedded with the epoxy resin, thus constituting a composite interlayer with an average thickness between the two electrodes of 0.7 ± 0.1 mm. The lower experimental thickness (3.2 mm) compared to the barely sum of the various layers (3.6 mm as the total sum of 10 GFRP plies of 2.7 mm, 2 brass sheets electrodes of 0.1 mm each and PZT nanofibrous interlayer of 0.7 mm) can be ascribed to the fixed amount of resin which was shared between the GFRP plies and the PZT nanofibers interlayer. Externally, the two brass sheets electrodes (visible as bright layers in Fig. 8a) are stacked. The embedding of the nanofibers in the epoxy matrix can be observed in high-magnification SEM images. In particular, in Fig. 8c it is clearly shown how the PZT nanofibers are fully embedded in the surrounding epoxy resin, without any macroscale discontinuity between them, which instead occurs in the case of integration of a commercial bulky PZT disk. Indeed, it can be assumed that there is no separation between the epoxy resin of the two GFRP layers within the electrodes, thanks to the high porosity of the nanofibrous membrane, which is fully impregnated by the resin during the curing cycle described in Section 2.2.1. These assumptions are also confirmed by the SEM magnification of Fig. 8d, where the glass microfibers of the GFRP and the PZT nanofibers appear in intimate contact. Based on these findings, the volumetric fraction of the PZT nanofibers v_p between the two brass sheets electrodes can be determined. From Fig. 8c, the volumetric fraction of the nanofibers within the epoxy resin meatus was assessed via ImageJ. Subsequently, by considering the adjacent GFRP plies shown in Fig. 8a, the resulting value of v_p was calculated as 0.23.

3.3. Electromechanical properties of the laminates

The piezoelectric output voltages of a of both PZT nf and PZT disk composite laminates were measured with the acquisition circuit described in [36], and they are reported Fig. 9a and Fig. 9b, respectively.

The piezoelectric sensitivity S (mV/N) of each laminate was calculated as the ratio between the peak-to-peak output voltage (blue curve) and the peak-to-peak sinusoidal compressive force (red curve), which was applied on the sensing portions of the panels at a frequency of 10 Hz. According to the measured capacity values (C), the cutoff frequency f_c has been evaluated for each sensor as $f_c=1/2\pi RC$, where the time constant RC was evaluated as described in [36]. Afterward, the piezoelectric strain coefficient d_{33} was calculated according to Equation (1).

The aforementioned electric properties are reported in Table 1 both for the PZT nf and PZT disk laminate panels, as the mean value μ and the relative confidence interval of 95.4 % (μ-2σ, μ + 2σ), where σ is the standard deviation of the electrical properties measured on the four sensors. Note that for the derived value d_{33}, the confidence interval was calculated considering the error propagation.

The piezoelectric strain coefficient d_{33} of the PZT_disk sensors is four orders of magnitude higher than the PZT_nf one. However, the sensitivity of the PZT_nf sensor is only one order of magnitude lower than that of the PZT_disk one, given the lower capacity values. This difference is mainly attributable to the configuration of the commercial PZT disks. Indeed, one surface of the PZT commercial disk is bonded on a brass sheet electrode, and the other one is covered by a thin metallization. In this way, the electrodes are directly in contact with the piezoelectric ceramic disk and the electric charges are collected immediately once a compressive force is applied. On the contrary, in the PZT nf composite plate, the piezoelectric nanofibers are embedded in the electrical insulating epoxy matrix so that the electric charges have to flow through the electrically insulating epoxy resin before reaching the signal electrodes. Moreover, according to [39], the d_{33} value of the piezoelectric nanofibers is lower than the d_{33} of the bulky disk, because during the polarization process the electric field was partially applied on the PZT nanofibers, due to the high resistivity of the GFRP plies. Consequently, the piezoelectric output of the composite material is affected by the d_{33} of the PZT nanofibers, the dielectric permittivity and the volumetric fractions of the two phases between the electrodes, as described in [39, 55].

Table 1
Electrical properties of the PZT nf and PZT disk composite laminates. The values are reported with a confidence interval of 95.4 %.

		PZT_disk	PZT_nf
C (F)	**Mean**	$5.18*10^{-9}$	$1.05*10^{-11}$
	Confidence interval	[5.08, 5.28] $*10^{-9}$	[0.81, 1.29] $*10^{-11}$
	Relative error	1.93 %	23.33 %
f_c (HZ)	**Mean**	$3.07*10^{-3}$	1.53
	Confidence interval	[3.02, 3.14] $*10^{-3}$	[1.16, 1.90]
	Relative error	1.95 %	24.22 %
S (mV/N)	**Mean**	28.34	2.97
	Confidence interval	[25.65, 31.02]	[2.65, 3.29]
	Relative error	9.47 %	10.71 %
d_{33}(pC/N)	**Mean**	$1.47*10^{2}$	$3.11*10^{-2}$
	Confidence interval	[1.32, 1.61] $*10^{2}$	[2.32, 3.92] $*10^{-2}$
	Relative error	9.67 %	25.67 %

The proposed composite materials fall within the broader class of self-sensing piezoelectric laminates. Their performance is influenced by the quantity and type of piezoelectric elements interleaved, the nature of the embedding matrix, and the electrode configuration. Table 2 provides an overview of these laminates, highlighting their sensitivity (defined as the ratio between output voltage and applied force in compression tests), along with their piezoelectric strain coefficient d_{33} and voltage coefficient g_{33}.

3.4. Impact localization performances

In Fig. 10, time domain signals generated by pencil lead break excitation are reported for the PZT disk (left) and PZT nf (right) plates. The coloured dots represent the raw signals measured by the three sensors, while the continuous black curves are the signal filtered.

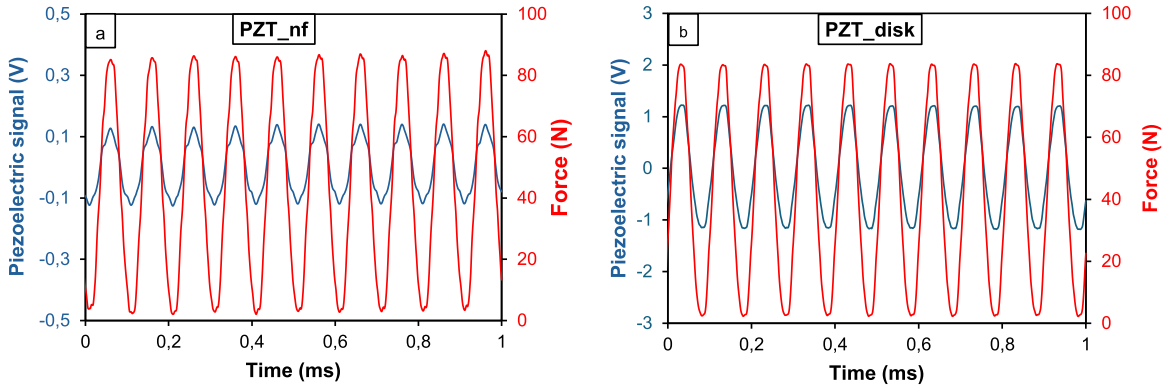

Fig. 9. . Piezoelectric output voltage of the (a) PZT_nf and (b) PZT_disk composite laminates.

Table 2
Comparison of the performances of different typology of piezoelectric self-sensing composite materials.

Self-sensing laminate		Sensitivity (mV/kN)	d_{33} (pC/N)	g_{33} (Vm/N)	Ref
Piezoelectric element	Composite laminate				
PZT Disk	GFRP	$28.3*10^3$	$1.5*10^2$	$9.2*10^{-3}$	This work
PZT MicroPowder (14 %vol)	GFRP	$3.6*10^3$	$5.2*10^{-2}$	$7.2*10^{-3}$	[39]
PZT MicroPowder (24 %vol)	GFRP	$8.6*10^3$	$23.7*10^{-2}$	$2.3*10^{-3}$	[39]
PZT MicroPowder (39 %vol)	GFRP	$12.4*10^3$	$55.6*10^{-2}$	$4.1*10^{-3}$	[39]
PZT NanoFiber	GFRP	$2.9*10^3$	$7.5*10^{-2}$	$5.7*10^{-4}$	This work
PVDF-TrFE Film	No embedding	$29.3*10^4$	22	$2.3*10^{-1}$	[56]
PVDF-TrFE NanoFiber	GLARE	24.8	$5.1*10^{-3}$	$1.2*10^{-4}$	[57]
PVDF-TrFE NanoFiber	CuCFRP	39.1	$2.7*10^{-3}$	$4.5*10^{-5}$	[58]
PVDF-TrFE NanoFiber	CFRP	$3.5*10^2$	$5.0*10^{-1}$	$9.4*10^{-3}$	[59]

Indeed, as already investigated in previous works [50], the presence of signal noise can hamper the successful estimation of the ToA. To prevent this issue, a dedicated pre-processing stage instrumental to enhance the signal-to-noise ratio of the input data has been applied, before the AIC algorithm. The pipeline consists of three steps: i) detrend, necessary to remove DC values and straight-fit line associated with sensor drift, ii) moving median filtering with a sliding window of 100 samples, empirically determined to be the optimal quantity to remove high frequency spurious spectral components, and iii) signal smoothing based on a Savitzky-Golay filter. The outcomes of such data pre-elaboration are plotted in Fig. 10 in the black curves, superimposed to the coloured profiles which represent, instead, raw data acquired from the embedded transducers.

Noteworthy, the trend in the generated wave is clearly visible in both types of sensors. The most remarkable difference is the amplitude of the received signals. Indeed, while a maximum average peak-to-peak voltage of 250 mV_{pp} has been measured for PZT disk, the same quantity decreases to 80 mV_{pp} for the PZT nf plate, consistently with the sensitivity values reported in Table 1. This difference can be attributable to two major causes. The first is an electrical aspect related to the lower d_{33} of the PZT nanofibers and the presence of the dielectric material (GFRP), as described in Section 3.3. The second is a mechanical aspect related to the different geometries and elastic properties of the sensing materials between the electrodes, which likely result in different electromechanical resonance frequencies with respect to the PZT disk ones.

Besides, the identified ToAs values returned by the AIC algorithm (marked as dotted vertical lines and magenta markers) are well aligned with the temporal points corresponding to the transition between a low-variance (i.e., absence of signal) and high-variance (i.e., presence of signal) regions. It is worth highlighting that within the framework of the proposed technology, only the first-arriving wave is of significance, as the method exclusively considers the earliest signal in time. Accordingly, any subsequent reflections, even if they occur, are not taken into account.

Additionally, the frequency content of the registered signals measured by the embedded transducers per generated AE event has been analyzed. However, since the Fast Fourier Transform does not contain temporal information which is, instead, paramount in our case to distinguish the arrival of different spectral components having different spectral energy, the time-frequency transform has been first computed, to precisely correlate the signal energy to the ToA and identify the spectral regions of interest. Then, the power spectral density of the signals has been extracted and a comparative analysis between multiple sensing positions has been performed, as shown in Fig. 11. The time-frequency trends for the AE signals of Fig. 10 are plotted along with the spectrum analysis obtained with the Chirpz transform limited to the 1-100 kHz where all the signal content is contained. This spectrum analyzer has been preferred over basic Fourier-based transformations to improve the spectral resolution in the sought frequency band of interest. As can be seen, there is quite a broad variation in the location, width, and shape of the main lobe associated with the ToA, as it depends on the specificity of the impact test and on the sensitivity of the sensing element. Indeed, comparing the PZT nf and the PZT disk panels, a different damping effect on the acquired signal is observable, as proved by spectral content which extend beyond 10 kHz for the commercially embedded transducers. Conversely, the nanofibrous sensor induces a low-pass effect which removes all the components below 20 kHz. Besides these discrepancies, one can notice that, in both cases, most of the signal energy is carried by a couple of travelling waves at the frequency below 10 kHz, consistent with the type of generated excitation (PLB test). Note that, even if the main peak is most often attributable to the onset time, this is not always the case depending on the nature of the travelling wave mode.

Finally, starting from these ToAs estimations, the positions of the impacted locations were determined, obtaining the results shown in Fig. 12, in which the target (round marker) and the computed (cross marker) impact points are shown. The average localization error, defined as the absolute difference between the true d and the estimated

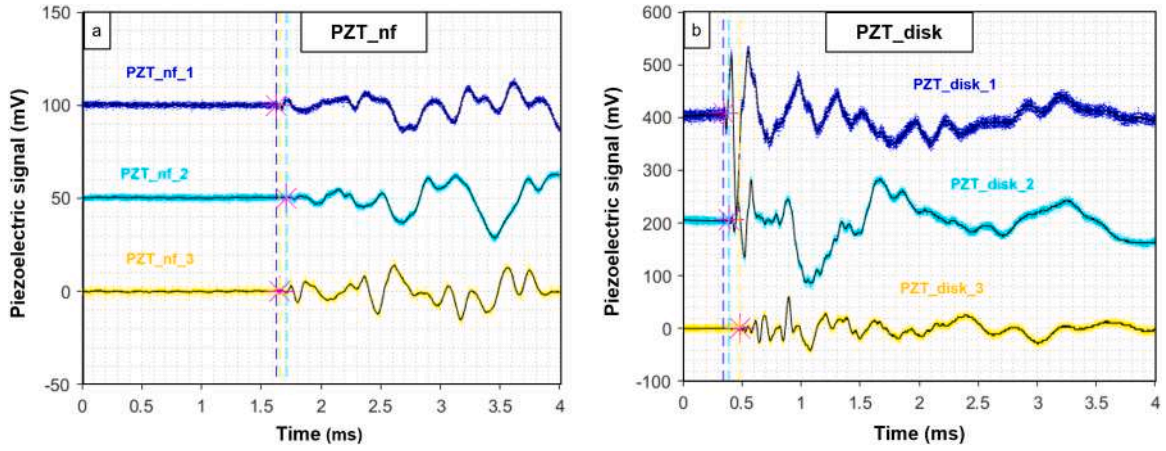

Fig. 10. Time waveforms registered during an impact localization test for the (a) PZT_nf and (b) PZT_disk plates.

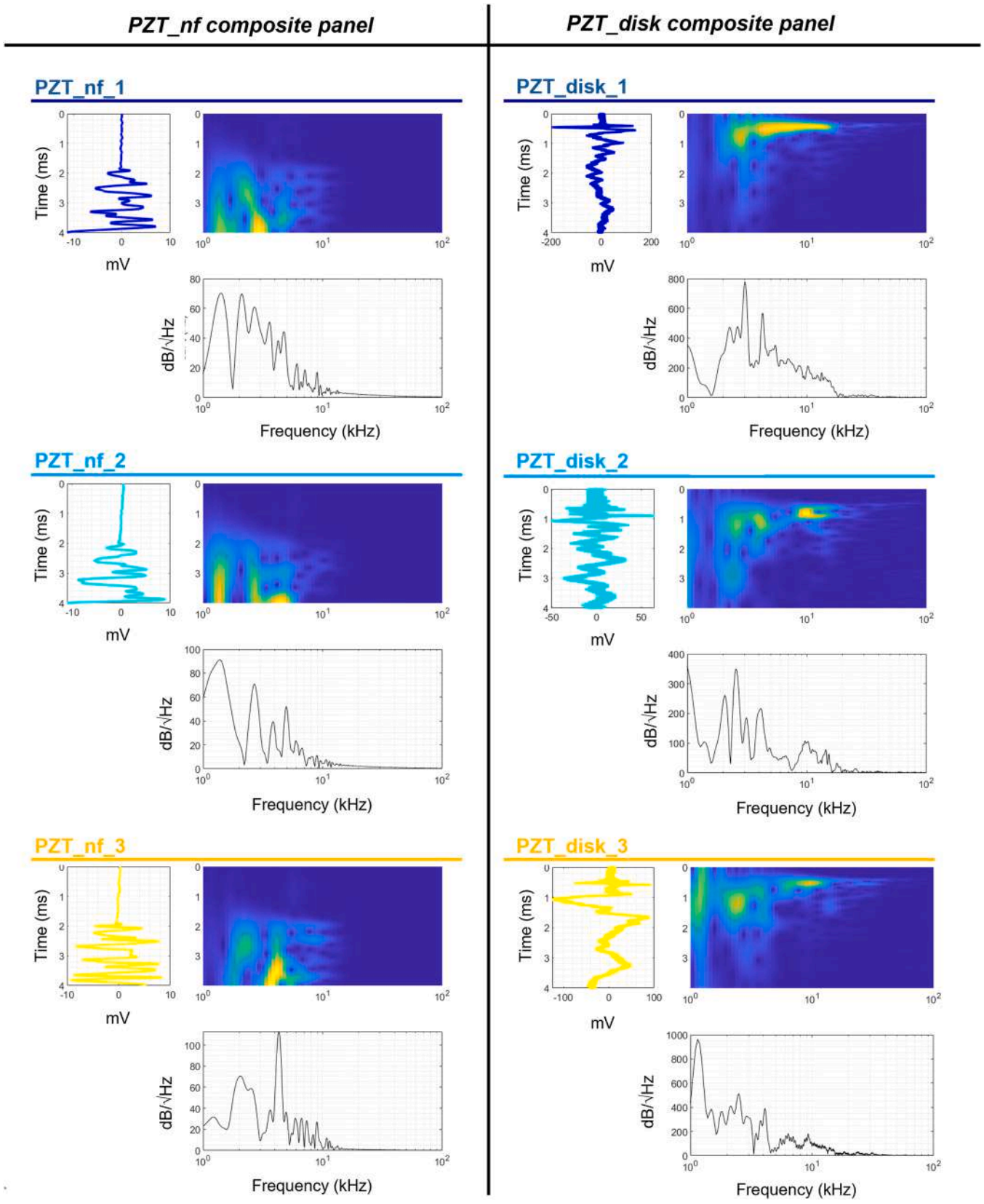

Fig. 11. Power spectral density of the signals received from each sensor of the panel, both for PZT_nf and PZT_disk.

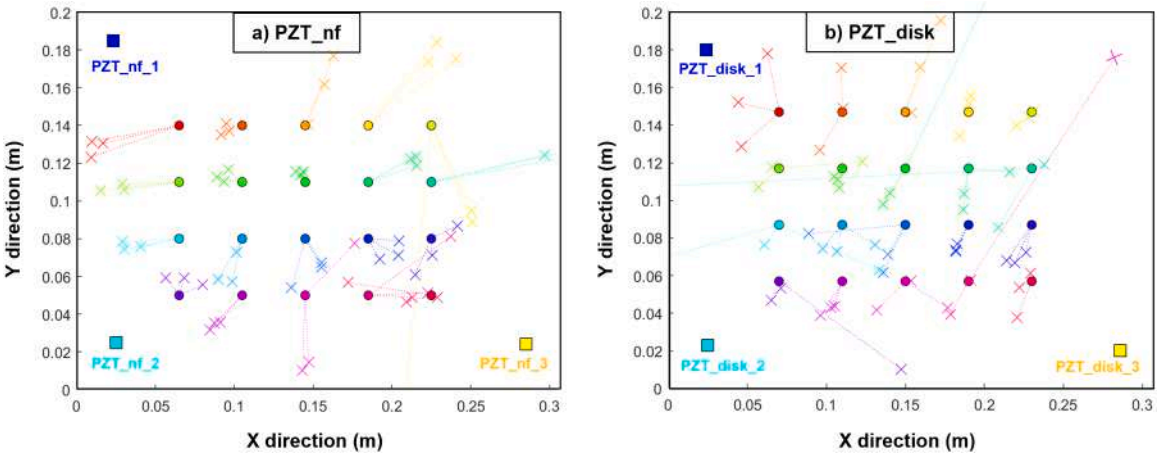

Fig. 12. Geometrical representation of the 20 impact positions (round markers) versus the estimated impact positions (cross markers) for both the (a) PZT_nf and (b) PZT_disk composite panels.

$\widehat{d}$ distance, has been computed for each impact position upon three repetitions. Referring to the geometry of the panels of Fig. 12, the impact positions have been numbered as shown in Table 3, and the corresponding localization error is reported both for the PZT disk and PZT nf panels. The total average localization error amounts to 2.50 ± 2.46 cm for the PZT disk, while it reaches 3.74 ± 2.84 cm for the PZT nf panels. By considering only the internal impact points of the grid, which are further from the boundaries, the average localization error lowers to 2.06 ± 0.65 cm and 1.93 ± 1.56 cm for PZT nf and PZT com, respectively. With respect to the PZT nf panel, the lower impact localization error of the PZT disk can be mainly attributed to the higher sensitivity (see Table 1), which enables a better estimation of the ToA by measuring output signals with higher amplitude, as visible in Fig. 10.

3.5. Impact resistance

The impact resistance of the composite laminates was evaluated by means of low-velocity impact tests described in Section 2.3.3. In Fig. 13 the impact force vs displacement curves are plotted for each laminate and impact energy (3 J, 6 J and 9 J). In Fig. 14 the absorbed energy values are calculated for each curve. Furthermore, the optical micrograph analyses (Fig. 15) were performed to directly assess the damaged zone.

According to Fig. 13, the stiffness of the three different types of laminates are comparable, as the initial slope of the force vs displacement curves are similar. Indeed, the pristine GFRP laminate was expressly fabricated by tuning the number of GFRP plies in order to have the same thicknesses of the PZT disk and the PZT nf ones. Considering the curves of the pristine GFRP and the PZT nf laminates, no significant force drops are observable, and the curves are comparable for all three levels of impact energy. On the other hand, the PZT_disk laminate presents a force drop between 2.5 and 3 kN for all the impact energies, which can be associated with high energy damages, such as fiber breakage and extended delamination.

The abovementioned behaviors are confirmed by the absorbed energy values reported in the bar graph of Fig. 14. Generally, the PZT_disk laminates present the highest values of absorbed energy for all the three energy levels, whereas the absorbed energy is the lowest for impacts occurring on the pristine GFRP laminates. The PZT_nf laminates always show intermediate behavior. During impact, viscous damping, fiber breakage and plasticization are the main causes of energy absorption [1]. In the case of PZT_disk and PZT_nf, the brass electrodes could plasticize and absorb energy, thus leading to a major difference with respect to the pristine GFRP in the bar graph of Fig. 14.

To investigate the delamination regions and to observe how the piezoelectric layers (both ceramic disk and PZT nanofibers) responded to the mechanical impacts, optical micrograph analyses of the cross-sections of the pristine GFRP, PZT_disk and PZT_nf laminates were performed. In Fig. 15a, the micrographs are arranged in a matrix-like pattern, where the first row refers to the micrographs of the not-impacted laminates, and the following ones correspond to the three levels of impact energy. Only half of the micrographs are shown, as damages induced by the impacts are symmetric with respect to the impact axis. Furthermore, SEM micrograph magnifications of the red highlighted areas are reported to deeply investigate the differences between the integration of the PZT commercial disk and the PZT nanofibers.

At 3 J impact, the pristine GFRP laminate does not present any cracks, as well as the PZT_nf. Differently, 45° oriented cracks are visible in the ceramic disk of the PZT_disk laminate, which promote delamination between the PZT disk and the brass electrode.

For the 6 J energy impact, the pristine GFRP laminate does not present any visible cracks. Conversely, the PZT_disk shows a complete debonding between the PZT ceramic layer and the brass electrode, due to a large number of cracks developed in the PZT. Moreover, the debonding between the GFRP ply and the electrode is visible. The

Table 3
Average localization errors (cm) calculated for all the 20 impact positions, both for the PZT disk and PZT nf composite panels.

PZT nf Average localization error: 3.74 ± 2.84 cm					**PZT disk** Average localization error: 2.50 ± 2.46 cm				
1st	**2nd**	**3rd**	**4th**	**5th**	**1st**	**2nd**	**3rd**	**4th**	**5th**
6.11 ± 0.41	1.82 ± 0.26	1.87 ± 1.05	5.13 ± 0.64	9.48 ± 5.08	2.79 ± 0.72	1.93 ± 0.86	3.25 ± 2.46	1.02 ± 0.68	0.67 ± 0.24
6th	**7th**	**8th**	**9th**	**10th**	**6th**	**7th**	**8th**	**9th**	**10th**
4.64 ± 0.67	1.78 ± 0.31	0.87 ± 0.19	2.47 ± 0.16	12.76 ± 4.36	2.31 ± 2.54	0.46 ± 0.16	5.10 ± 5.91	1.78 ± 1.03	10.56 ± 14.07
11th	**12th**	**13th**	**14th**	**15th**	**11th**	**12th**	**13th**	**14th**	**15th**
3.85 ± 0.49	2.79 ± 0.79	2.63 ± 0.68	1.85 ± 0.18	1.94 ± 0.80	2.57 ± 3.18	1.36 ± 0.88	2.33 ± 2.34	0.54 ± 0.29	0.82 ± 0.48
16th	**17th**	**18th**	**19th**	**20th**	**16th**	**17th**	**18th**	**19th**	**20th**
0.88 ± 0.45	3.19 ± 0.32	4.11 ± 0.59	3.69 ± 1.21	2.97 ± 2.06	3.40 ± 4.08	0.73 ± 0.51	0.76 ± 0.57	6.92 ± 8.33	0.66 ± 0.37

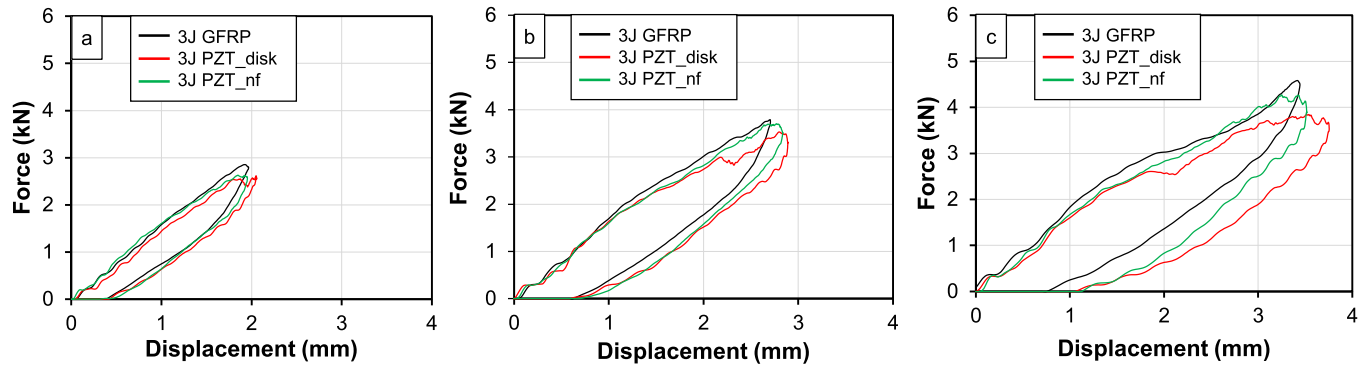

Fig. 13. Low-velocity impact tests: impact contact force vs. displacement response at (a) 3 J, (b) 6 J and (c) 9 J.

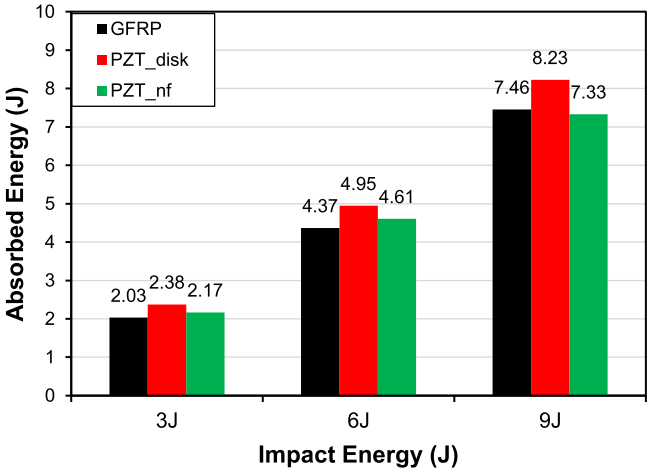

Fig. 14. Absorbed energy for low-velocity impact tests at 3 J, 6 J and 9 J.

delamination caused a decrease of the bending strength of the laminate, which led to fiber breakage in the bottom layer of the laminate. Debonding between the GFRP layers and the brass electrodes is also visible for the PZT_nf impacted at 6 J, whereas the piezoelectric nanofibrous layer does not show any kind of visible cracks. In this case, the delamination extension is not enough to reduce the bending strength of the laminate so that there is no fiber breakage in the bottom layer. These findings are also confirmed by the SEM images of Fig. 15b and Fig. 15d for the PZT_disk and PZT_nf, respectively. From those micrographs, the debonding between the brass electrodes and the GFRP layers is clearly visible in both cases (some detritus originated during the polishing process slipped into the debonded region). However, considering the active layers, in the case of PZT_disk, multiple diagonal cracks are present in the ceramic disk, whereas no visible cracks are detected in the nanofibrous layer.

In the case of the 9 J energy impact, the pristine GFRP composite material presents some small cracks which lead to visible delamination, as indicated by the red arrows of Fig. 15a. Similarly to the 6 J impact, the PZT_disk laminate impacted at 9 J shows a large amount of fiber breakage in the bottom layers of the laminate, due to debonding between GFRP and the brass electrodes and cracks in the PZT ceramic disk, which leads to a reduction of the bending strength. Fiber breakage in the lower part of the PZT_nf laminate is also observable, but they are less than the PZT_disk ones. Indeed, as observable in the SEM micrographs of Fig. 15c and Fig. 15e, while the PZT_disk presents both debonding of the brass electrode and ceramic disk fractures, the PZT_nf only shows debonding between the GFRP layer and the electrodes. No cracks are visible in the nanofibrous region, and this is a remarkable aspect that positively encourages the use of PZT nanofibers instead of bulky ceramic disks for SHM applications. The weak component of the PZT_nf sensor seems to be the brass electrodes, which plasticize and debond from the GFRP.

4. Conclusions

In this work, PZT nanofibers were interleaved within the plies of a GFRP composite laminate (PZT_nf) for elastic wave monitoring and impact localization. These diagnostic techniques traditionally rely on the integration of fragile ceramic PZT sensors, which detrimentally affect the mechanical properties of the laminate. This research introduces an innovative approach for elastic waves monitoring by employing PZT nanofibers, which combine the exceptional piezoelectric performance of PZT with the minimal impact of nanostructured materials on the mechanical integrity of the laminate.

Specifically, the nanofibers were embedded in the four corners of the composite panel (30 × 20 cm), thus defining the perimeter of a sensing area where the mechanical impact occurs. The polarized PZT nanofibers successfully detected the propagation of elastic waves, and their piezoelectric signals were utilized to localize the impact position via a triangulation algorithm. For comparison, a counterpart GFRP laminate with commercial PZT disk interleaved (PZT_disk) was also fabricated. Although PZT_nf exhibited lower sensing performance (sensitivity, d_{33} and g_{33}), it was still able to effectively perform impact localization, with localization error of 3.74 ± 2.84 cm versus the 2.50 ± 2.46 cm of the PZT_nf. It should be noted that optimizing the number and distribution of sensors could substantially reduce errors. Moreover, since sensitivity depends on the volumetric fraction of PZT nanofibers within the GFRP plies, enhancing sensing performance could further improve localization accuracy.

From a mechanical perspective, the PZT nanofibrous membranes demonstrated advantages over commercial ceramic PZT disks, as evidenced by the low-velocity impact tests. The brittle nature of the ceramic PZT led to fractures on the PZT disks, which triggered delamination even for the lowest impact energy level (3 J). Conversely, the intimate integration of the PZT nanofibers within the epoxy matrix of GFRP prevented any crack initiation in the nanofibrous layer even at 9 J of impact energy, whereas the primary cause of debonding was identified as the brass electrodes.

The proposed self-sensing laminate serves as a proof of concept for a novel class of composite materials suitable for impact localization techniques, owing to the PZT nanofibers that conjugate high sensitivity with low mechanical intrusiveness. At this stage, the main limitation of the proposed technology is related to the operating temperatures, which should not exceed the Curie temperature of the piezoelectric material to not lose the permanent polarization. Moreover, since the brass sheet electrodes represent the main cause of delamination, future developments could include the use of alternative signal collection methods, such as exploiting the electrical conductivity of carbon fibers in CFRP laminates. However, differently from rigid PZT disks, the

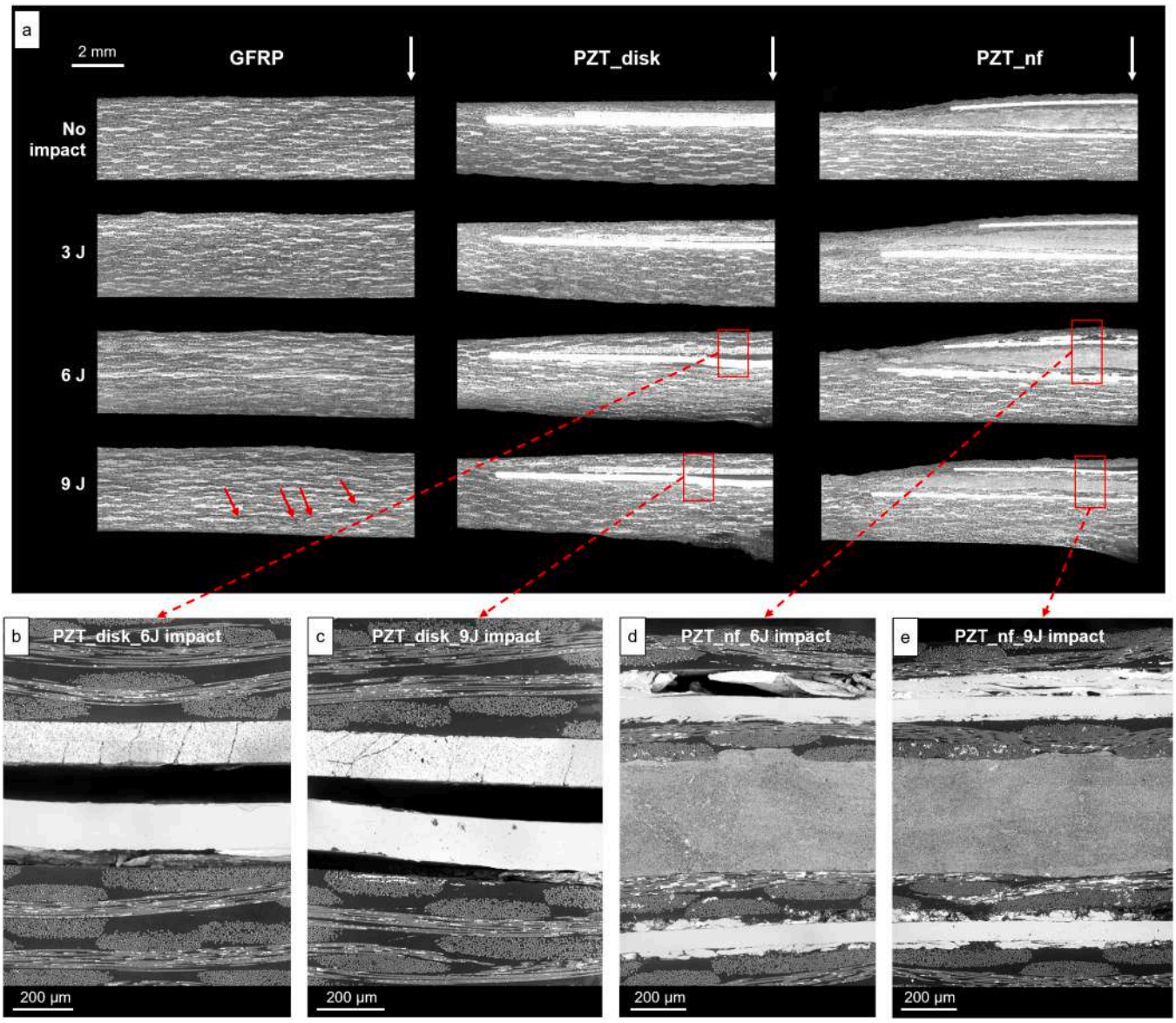

Fig. 15. a) Optical micrograph analyses of the cross-section of the composite laminates, and SEM magnification of the b) PZT_disk at 6 J, c) PZT_disk at 9 J, d) PZT_nf at 6 J and e) PZT_nf at 9 J.

possibility to bend and model the nanofibrous membrane could also pave the way for a variety of engineering applications, such as self-sensing laminates with single or double curvature geometries, aerospace structures such as the fuselage or wings. In those cases, an appropriate tuning of the triangulation method and the ToA estimation would be necessary, considering both the geometry and the embedding matrix.

Footnotes

1. https://www.sigmaaldrich.com;
2. https://www.carloerbareagents.com;
3. http://www.spinbow.it;
4. https://www.spellmanhv.com;
5. https://www.kdscientific.com;
6. https://www.murata.com/en-eu;
7. https://www.delta-preg.com;
8. https://www.xppower.com/fug-guth-high-voltage;
9. https://linmot.com;
10. https://www.ndt.net/article/az/ae/hsunielsensource.htm#:~:text=NDT%20Encyclopedia%20%2D%20Acoustic%20Emission%20(AE):%20Hsu%2DNielsen%20source&text=Device%20(named%20after%20developer%20of,for%20the%20object%20being%20monitored.

CRediT authorship contribution statement

Giacomo Selleri: Writing – original draft, Methodology, Investigation, Formal analysis, Conceptualization. **Maria Elena Gino:** Writing – original draft, Methodology, Investigation, Conceptualization. **Federica Zonzini:** Writing – original draft, Methodology, Investigation. **Luca De Marchi:** Supervision, Funding acquisition, Conceptualization. **Maria Letizia Focarete:** Writing – review & editing, Supervision, Funding acquisition, Conceptualization. **Davide Fabiani:** Supervision, Funding acquisition, Conceptualization. **Andrea Zucchelli:** Writing – original draft, Supervision, Funding acquisition, Formal analysis, Conceptualization. **Tommaso Maria Brugo:** Writing – original draft, Project administration, Methodology, Investigation, Formal analysis, Conceptualization.

Declaration of competing interest

The authors declare that they have no known competing financial interests or personal relationships that could have appeared to influence the work reported in this paper.

Acknowledgments

This research was funded by PNR - Alma Idea 2022 (CUP J45F21002000001), European Union's Horizon 2020 Research and Innovation Programme "MyLeg" (No. 780871, 2018), by the European Union - NextGenerationEU - National Sustainable Mobility Center (CN00000023) Spoke 11 - Innovative Materials & Lightweighting and the Project Ecosyster - Ecosystem for Sustainable Transition in Emilia-Romagna (CUP J33C22001240001). The opinions expressed are those of the authors only and should not be considered as representative of the European Union or the European Commission's official position. Neither the European Union nor the European Commission can be held responsible for them.

Appendix A

The sensitivity, the piezoelectric strain coefficient d_{33} and the piezoelectric voltage coefficient g_{33} have been evaluated based on the equivalent electric circuit described in this section.

The piezoelectric element was modeled as a charge generator q_p in parallel with its capacitance C_p and its resistance R_p, as shown in Figure A.1. C_p is the capacitance of the cables (~5 pF), and the instrumentation amplifier INA118P is used for the signal acquisition (high input resistance $R_{in} = 10$ GΩ). Such equivalent electric circuit is an RC circuit, where $R = (R_{in} * R_p)/(R_{in} * R_p)$ and $C = C_p + C_c$ and whose cut-off frequency depends on the RC time constant.

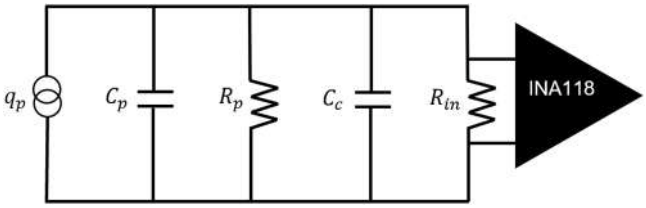

Figure A.1. . Equivalent circuit of the piezoelectric laminate connected to a voltage amplifier.

By applying Kirchhoff's laws, the output voltage measured across R_{in} can be written as:

$$V(t) = \frac{R}{j\omega RC + 1} d_{33} \frac{dF}{dt} \tag{A.1}$$

where F is the applied force. In the case of a sinusoidal load F(t)=F * sin (ωt), where $\omega = 2\pi/T$ and T is the period, the Equation (A.1) can be solved in the Laplace domain and anti-transformed back in the time domain, as shown in Equation (A.2) [35].

$$V(t) = \frac{F\omega R d_{33}}{\omega^2 R^2 C^2 + 1} \left(- e^{-t}/RC + \cos(\omega t) + \omega RC sin(\omega t) \right) \tag{A.2}$$

The d_{33} value of the piezoelectric element can be calculated from Equation (A.2), and the piezoelectric voltage coefficient g_{33} can be calculated as $g_{33} = g_{33}/\varepsilon_p$, where ε_p is the dielectric constant of the piezoelectric layer. In the case of high RC values compared to the period of the applied force - which has an angular frequency ω the exponential term and the first steady-state one can be neglected and Equation (A.2) can be simplified as Equation (1).

Data availability

Data will be made available on request.

References

[1] Serge Abrate, Impact on Composite Structures, Cambridge University Press, 2005.
[2] D.D.L. Chung, A review of multifunctional polymer-matrix structural composites, Compos. Part B Eng. 160 (November 2018) 644–660, https://doi.org/10.1016/j.compositesb.2018.12.117, 2019.
[3] K. Schulte, C. Baron, Load and failure analyses of CFRP laminates by means of electrical resistivity measurements, Compos. Sci. Technol. 36 (1) (1989) 63–76, https://doi.org/10.1016/0266-3538(89)90016-X.
[4] S. Wang, D.D.L. Chung, Self-sensing of flexural strain and damage in carbon fiber sspolymer-matrix composite by electrical resistance measurement, Carbon N. Y. 44 (13) (2006) 2739–2751, https://doi.org/10.1016/j.carbon.2006.03.034.
[5] S. Wang, D.P. Kowalik, D.D.L. Chung, Self-sensing attained in carbon-fiber-polymer-matrix structural composites by using the interlaminar interface as a sensor, Smart Mater. Struct. 13 (3) (2004) 570–592, https://doi.org/10.1088/0964-1726/13/3/017.
[6] Z. Shen, H. Zhou, Mechanical and electrical behavior of carbon fiber structural capacitors: effects of delamination and interlaminar damage, Compos. Struct. 166 (2017) 38–48, https://doi.org/10.1016/j.compstruct.2016.12.062.
[7] L. Vertuccio, L. Guadagno, G. Spinelli, P. Lamberti, V. Tucci, S. Russo, Piezoresistive properties of resin reinforced with carbon nanotubes for health-monitoring of aircraft primary structures, Compos. Part B Eng. 107 (2016) 192–202, https://doi.org/10.1016/j.compositesb.2016.09.061.
[8] J. Yan, A. Downey, A. Chen, S. Laflamme, S. Hassan, Capacitance-based sensor with layered carbon-fiber reinforced polymer and titania-filled epoxy, Compos. Struct. 227 (2019) 111247, https://doi.org/10.1016/j.compstruct.2019.111247. July.
[9] H. Rocha, C. Semprimoschnig, J.P. Nunes, Sensors for process and structural health monitoring of aerospace composites: A review, Eng. Struct. 237 (2020) 2021, https://doi.org/10.1016/j.engstruct.2021.112231. July.
[10] C. Tuloup, W. Harizi, Z. Aboura, Y. Meyer, K. Khellil, R. Lachat, On the use of in-situ piezoelectric sensors for the manufacturing and structural health monitoring of polymer-matrix composites: A literature review, Compos. Struct. 215 (2019) 127–149, https://doi.org/10.1016/j.compstruct.2019.02.046. February.
[11] S.M.A. Musa, M.H. Dzulkifli, A.I. Azmi, S.A. Ibrahim, Embedded and surface-mounted Fiber bragg grating as a multiparameter sensor in Fiber-reinforced polymer composite materials: A review, IEEE Access 11 (2023) 86611–86644, https://doi.org/10.1109/ACCESS.2023.3304679. August.
[12] Y. Liao, P. Zhou, D. Pan, L.M. Zhou, Z. Su, An ultra-thin printable nanocomposite sensor network for structural health monitoring, Struct. Heal. Monit. 20 (3) (2021) 894–903, https://doi.org/10.1177/1475921719859338.
[13] Y. Su, et al., An implantable, compatible and networkable nanocomposite piezoresistive sensor for in situ acquisition of dynamic responses of CFRPs, Compos. Sci. Technol. 208 (2021) 108747, https://doi.org/10.1016/j.compscitech.2021.108747. February.

[14] B.W. Jang, Robust low-velocity impact localization algorithm on composite plate to dynamic operating conditions using fiber optic sensors, Compos. Struct. 280 (2022) 114881, https://doi.org/10.1016/j.compstruct.2021.114881.
[15] J. Byeong-Wook, L. Yeon-Gwan, K. Yoon-Young, K. Jin-Hyuk, K. Chun-Gon, Real-time impact identification algorithm for composite structures using fiber Bragg grating sensors, Struct. Control Heal. Monit. (May 2011), https://doi.org/10.1002/stc n/a-n/a2011.
[16] J. Yu, J. Liu, Z. Peng, L. Gan, S. Wan, Impact localization of composite structure based on SSA-CNN-LSTM using FBG sensors, IEEE Sens. J. 25 (7) (2025) 11063–11074, https://doi.org/10.1109/JSEN.2025.3540461.
[17] B.W. Jang, C.G. Kim, Real-time detection of low-velocity impact-induced delamination onset in composite laminates for efficient management of structural health, Compos. Part B Eng. 123 (2017) 124–135, https://doi.org/10.1016/j.compositesb.2017.05.019.
[18] A. Annunziato, F. Anelli, J. Gates, C. Holmes, F. Prudenzano, Design of polarization-maintaining FBGs using polyimide films to improve strain-temperature sensing in CFRP laminates, IEEE Photonics J 13 (2) (2021), https://doi.org/10.1109/JPHOT.2021.3063172.
[19] J. Chen, J. Wang, X. Li, L. Sun, S. Li, A. Ding, Monitoring of temperature and cure-induced strain gradient in laminated composite plate with FBG sensors, Compos. Struct. 242 (2020) 112168, https://doi.org/10.1016/j.compstruct.2020.112168. February.
[20] A. Lamberti, G. Luyckx, W. Van Paepegem, A. Rezayat, S. Vanlanduit, Detection, localization and quantification of impact events on a stiffened composite panel with embedded fiber bragg grating sensor networks, Sensors (Switzerland) 17 (4) (2017) 1–13, https://doi.org/10.3390/s17040743.
[21] T. Okabe, S. Yashiro, Damage detection in holed composite laminates using an embedded FBG sensor, Compos. Part A Appl. Sci. Manuf. 43 (3) (2012) 388–397, https://doi.org/10.1016/j.compositesa.2011.12.009.
[22] K. Shivakumar, A. Bhargava, Failure mechanics of a composite laminate embedded with a fiber optic sensor, J. Compos. Mater. 39 (9) (2005) 777–798, https://doi.org/10.1177/0021998305048156.
[23] D. Deng, et al., Multi-frequency probabilistic imaging fusion for impact localization on aircraft composite structures, Struct. Heal. Monit. 24 (1) (2025) 185–201, https://doi.org/10.1177/14759217241233181.
[24] D. Deng, et al., Data fusion based impact localization on aircraft composite structures using bayesian estimation and weighted averaging, Mech. Syst. Signal Process. 230 (2025) 112675, https://doi.org/10.1016/j.ymssp.2025.112675. March.
[25] D. Ai, D. Zhang, H. Zhu, Damage localization on reinforced concrete slab structure using electromechanical impedance technique and probability-weighted imaging algorithm, Constr. Build. Mater. 424 (2024) 135824, https://doi.org/10.1016/j.conbuildmat.2024.135824. March.
[26] D. Ai, D. Zhang, H. Zhu, A damage localization approach for concrete structure using discrete wavelet transform of electromechanical admittance of bonded PZT transducers, Mech. Syst. Signal Process. 218 (2024) 111531, https://doi.org/10.1016/j.ymssp.2024.111531. April.
[27] Y. Meyer, R. Lachat, G. Akhras, A review of manufacturing techniques of smart composite structures with embedded bulk piezoelectric transducers, Smart Mater. Struct. 28 (5) (2019), https://doi.org/10.1088/1361-665X/ab0fab.
[28] K.C. Jung, S.H. Chang, Advanced deep learning model-based impact characterization method for composite laminates, Compos. Sci. Technol. 207 (2021) 108713, https://doi.org/10.1016/j.compscitech.2021.108713. February.
[29] M. Saeedifar, J. Mansvelder, R. Mohammadi, D. Zarouchas, Using passive and active acoustic methods for impact damage assessment of composite structures, Compos. Struct. 226 (2019) 111252, https://doi.org/10.1016/j.compstruct.2019.111252. July.
[30] B. Yang, et al., Damage localization in composite laminates by building in PZT wafer transducers: A comparative study with surface-bonded PZT strategy, Adv. Eng. Mater. 21 (3) (2019) 1–12, https://doi.org/10.1002/adem.201801040.
[31] S. Masmoudi, A. El Mahi, S. Turki, Use of piezoelectric as acoustic emission sensor for in situ monitoring of composite structures, Compos. Part B Eng. 80 (2015) 307–320, https://doi.org/10.1016/j.compositesb.2015.06.003.
[32] S. Masmoudi, A. El, S. Turki, Fatigue behaviour and structural health monitoring by acoustic emission of E-glass /epoxy laminates with piezoelectric implant, Appl. Acoust. 108 (2015) 50–58, https://doi.org/10.1016/j.apacoust.2015.10.024.
[33] C. Andreades, P. Mahmoodi, F. Ciampa, Characterisation of smart CFRP composites with embedded PZT transducers for nonlinear ultrasonic applications, Compos. Struct. 206 (2018) 456–466, https://doi.org/10.1016/j.compstruct.2018.08.083. July.
[34] A. Huijer, C. Kassapoglou, L. Pahlavan, Acoustic emission monitoring of carbon fibre reinforced composites with embedded sensors for in-situ damage identification, Sensors 21 (20) (2021), https://doi.org/10.3390/s21206926.
[35] T.M. Brugo, et al., Self-sensing hybrid composite laminate by piezoelectric nanofibers interleaving, Compos. Part B Eng. 212 (October 2020) 108673, https://doi.org/10.1016/j.compositesb.2021.108673, 2021.
[36] G. Selleri, et al., Self-sensing composite material based on piezoelectric nanofibers, Mater. Des. 219 (2022) 110787, https://doi.org/10.1016/j.matdes.2022.110787.
[37] D. Fabiani, F. Grolli, M. Speranza, S.V. Suraci, T.M. Brugo, Piezoelectric nanofibers for integration in multifunctional materials, *2018*, IEEE Conf. Electr. Insul. Dielectr. Phenom. (2018) 14–17.
[38] H. Saghafi, T. Brugo, G. Minak, A. Zucchelli, The effect of PVDF nanofibers on mode-I fracture toughness of composite materials, Compos. Part B Eng. 72 (2015) 213–216, https://doi.org/10.1016/j.compositesb.2014.12.015.
[39] M.E. Gino, et al., On the design of a piezoelectric self-sensing smart composite laminate, Mater. Des. 219 (2022) 110783, https://doi.org/10.1016/j.matdes.2022.110783.
[40] M.Y. Hwang, L.H. Kang, Characteristics and fabrication of piezoelectric GFRP using smart resin prepreg for detecting impact signals, Compos. Sci. Technol. 167 (2018) 224–233, https://doi.org/10.1016/j.compscitech.2018.08.002. July.
[41] H.P. Konka, M.A. Wahab, K. Lian, The effects of embedded piezoelectric fiber composite sensors on the structural integrity of glass-fiber-epoxy composite laminate, Smart Mater. Struct. 21 (1) (2012), https://doi.org/10.1088/0964-1726/21/1/015016.
[42] T.I. Chang, S.C. Wang, C.P. Liu, C.F. Lin, J.L. Huang, Thermal behaviors and phase evolution of lead zirconate titanate prepared by sol-gel processing: the role of the pyrolysis time before calcination, J. Am. Ceram. Soc. 91 (8) (2008) 2545–2552, https://doi.org/10.1111/j.1551-2916.2008.02522.x.
[43] G. Yi, M. Sayer, An acetic acid/water based sol-gel PZT process II: formation of a water based solution, J. Sol-Gel Sci. Technol. 6 (1) (1996) 75–82, https://doi.org/10.1007/BF00402591.
[44] A.G. Gevorkyan, G.E. Shter, G.S. Grader, Rapid thermal processing of electrospun PbZr0.52Ti0.48O3 nanofibers, Thermochim. Acta 605 (2015) 107–114, https://doi.org/10.1016/j.tca.2015.03.001.
[45] N. Dharmaraj, C.H. Kim, H.Y. Kim, Pb(Zr0.5, Ti0.5)O3 nanofibres by electrospinning, Mater. Lett. 59 (24–25) (2005) 3085–3089, https://doi.org/10.1016/j.matlet.2005.05.040.
[46] O. Rozent, V.V. Beilin, G.E. Shter, G.S. Grader, Deformation control during thermal treatment of electrospun PbZr0.52Ti0.48O3 nanofiber mats, J. Am. Ceram. Soc. 99 (5) (2016) 1550–1556, https://doi.org/10.1111/jace.14203.
[47] G. Selleri et al., "Study on the polarization process for piezoelectric nanofibrous layers," in *2021 IEEE Conference on Electrical Insulation and Dielectric Phenomena (CEIDP)*, 2021, pp. 31–34.
[48] M. Sause, Investigation of pencil-lead breaks as acoustic emission sources, J. Acoust. Emiss. 29 (2011).
[49] B.G. Lopes, F.A. Alexandre, W.N. Lopes, P.R. De Aguiar, E.C. Bianchi, M.A.A. Viera, Study on the effect of the temperature in acoustic emission sensor by the pencil lead break test, 2018 13th IEEE Int. Conf. Ind. Appl. INDUSCON 2018 - Proc. (2019) 1226–1229, https://doi.org/10.1109/INDUSCON.2018.8627213.
[50] F. Zonzini, D. Bogomolov, T. Dhamija, N. Testoni, L. De Marchi, A. Marzani, Deep learning approaches for robust time of arrival estimation in acoustic emission monitoring, Sensors 22 (3) (2022) 1–21, https://doi.org/10.3390/s22031091.
[51] L. Capineri, A. Bulletti, Ultrasonic guided-waves sensors and integrated structural health monitoring systems for impact detection and localization: A review, Sensors 21 (9) (2021), https://doi.org/10.3390/s21092929.
[52] A. Wu, P.M. Vilarinho, I.M. Miranda Salvado, J.L. Baptista, Sol-gel preparation of lead zirconate titanate powders and ceramics: effect of alkoxide stabilizers and lead precursors, J. Am. Ceram. Soc. 83 (6) (2000) 1379–1385, https://doi.org/10.1111/j.1151-2916.2000.tb01397.x.
[53] S. Xu, Y. Shi, S.G. Kim, Fabrication and mechanical property of nano piezoelectric fibres, Nanotechnology 17 (17) (2006) 4497–4501, https://doi.org/10.1088/0957-4484/17/17/036.
[54] G. Zhang, X. Chen, W. Xu, W.D. Yao, Y. Shi, Piezoelectric property of PZT nanofibers characterized by resonant piezo-force microscopy, AIP Adv 12 (3) (2022), https://doi.org/10.1063/5.0081109.
[55] R.E. Newnham, D.P. Skinner, L.E. Cross, Connectivity and piezoelectric-pyroelectric composites, Mat. Res. Bull. 13 (1978) 525–536.
[56] Solvay, "Technical data sheet solvene 300 EAP electroactive polymer".
[57] T.M. Brugo, et al., Self-sensing hybrid composite laminate by piezoelectric nanofibers interleaving, Compos. Part B Eng. 212 (2021) 108673, https://doi.org/10.1016/j.compositesb.2021.108673. February.
[58] F. Mongioì, G. Selleri, T. Maria Brugo, E. Maccaferri, D. Fabiani, A. Zucchelli, Multifunctional composite material based on piezoelectric nanofibers and Cu-CFRP electrodes for sensing applications, Compos. Struct. 337 (September 2023) 118076, https://doi.org/10.1016/j.compstruct.2024.118076, 2024.
[59] F. Mongioì, G. Selleri, E. Maccaferri, D. Fabiani, A. Zucchelli, T.M. Brugo, CFRP laminate with autonomous sensing and enhanced impact resistance by P(VDF-TrFE) nanofibers interleaving, Compos. Part B Eng. 293 (November 2024) 112143, https://doi.org/10.1016/j.compositesb.2025.112143, 2025.